Experimental apparatus for universal spin-motion control in trapped multi-ion crystals

Donovan Webb

St Peter's College

University of Oxford

A thesis submitted for the degree of

Doctor of Philosophy

Trinity 2025

Contents

A Appendix   **42**

1
Motivation

2

Ion Trap Apparatus

Contents

A vast effort is spent on the initial build-up of the ion trap system, but throughout the life of the experiment, a greater effort is spent on its daily maintenance. I hope that this chapter will serve as a useful debugging-resource for future members of the FastGates team, and as a detailed recipe for anyone building a similar system.

Due to the size and complexity of the system, in this chapter we introduce an overview of the design, motivated by the desired functions. Many such ion trap experiment overviews exist in the theses of previous PhD generations, and so we will limit the discussion here to the unique features and capabilities of our system. As a map for this section we state the landmark features of an "ion trap" experiment. First, to confine the ions, static and dynamic electric fields are used which, due to
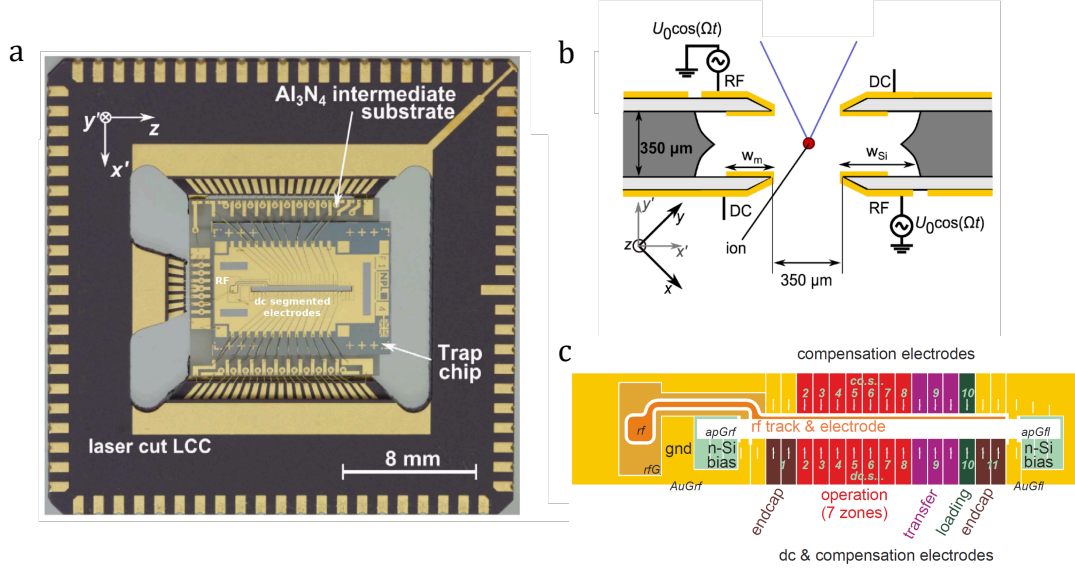
Figure 2.1: Schematics of the *NPL* trap chip used in this experiment. **a)** A front view of the trap chip. Axial confinement is provided by a subset of the segmented DC electrodes. Radial confinement is provided by the RF rails. **b)** A slice view of the trap. The red point here represents the ions, the gold are the RF and DC electrodes, and the grey is the silica substrate. It can be seen that the ion is $\sim 250\mu$m away from the nearest electrode. The numerical aperture of the ion due to the electrodes is ~ 0.71. **c)** A schematic of the electrode geometries and labelling for the front-face of the trap chip. A similar arrangement exists for the back-face. Figures from [1].

ions possesing non-zero electric charge, can provide trapping potentials, section 2.1.

Due to the fragility of the internal states of the ion (these are state -of-the-art sensors after all), we must take great care in isolating the ion from any noisy environment. This neccesitates the use of ultra-high vacuum (UHV) systems, section 2.3, vibration isolation, and magnetic shielding, section 2.2. To manipulate the internal electronic states of the ion, local electric and magnetic fields are created using RF antennae and, in this work, lasers, sections 2.4 and 2.4.1. Finally, to interface with the apparatus we have built, at the time scales set by our interaction strengths, we require a sophisticated and custom control system.

2.1   The Ion Trap

From Earnshaw's theorem, $\nabla^2 V = 0$, a stable stationary point in 3D cannot be realised using only static electric potentials, V, as if the potential is confining in two dimensions, it will be anticonfining in the third. Therefore, to achieve stable trapping, either an oscillating electric field (Paul trap [2]), or a static magnetic field (Penning trap [**<empty citation>**]) is used.

Recently, the microfabricated surface style linear Paul trap has gained popularity due to the maturity of chip fabrication technologies [3] and the potential route to scalability this offers [4]. In the surface trap, the 3D radial and axial electrodes of a "macro" trap are effectively projected onto a 2D surface. The stable confining point of such a trap is typically on the order of $50 - 100$ μm above the chip surface. The ease of fabrication of surface traps has allowed the creation of complex multizone devices with many DC electrodes. These multizone traps enable the shuttling of ions, a requirement for Quantum CCD type architectures [4]. However, this surface style geometry typically comes with two costs: the depth of the trapping potential is often greatly reduced, and the close proximity of the surface to the ion can be a large contributor to motional heating rates [5].

Our trap is provided by the *National Physical Laboratory* in the UK. This is a microfabricated 3D trap, which brings together the advantages of chip fabrication as well as the low heating rates and high trapping depths of a 3D style trap with greater ion-surface distances. Details on its design and characterisations can be found in [6, 7]. Figure 2.1 shows the electrode geometry of the trap and the relevant length scales. The ion-surface distance is now of the order 250 μm and we have demonstrated heating rates of 33(3) q/s on a 4 MHz radial mode (see section 3.3.2). An axial ion separation of ~ 5 μm is desired. For $^{40}\text{Ca}^+$ ions this means an axial mode frequency of $\omega_z \approx 2\pi \cdot 1.6$ MHz. This ion separation was chosen as a balance between the desire for high mode frequencies while keeping cross talk due to laser-addressing negligible.

The mode frequencies that can be achieved are ultimately limited by the breakdown voltage of the trap electrodes, $V_{\text{MAX}} = 400$ Vpp. Within this constraint, we are

targeting ~ 4 MHz for our radial frequencies. The choice of this higher frequency is motivated by several factors: the Doppler cooling limit is reduced, and the frequency separation between modes can be increased, which is useful for simplifying interactions involving motion.

In the following two sections we describe the experimental parameters used in our apparatus to achieve these mode frequencies.

2.1.1 Trap RF Chain

To utilise radial motional modes for low error quantum gates, we require the radio frequency (RF) field that produces the desired trapping pseudopotential to be both frequency and amplitude stable. Our *NPL* trap is rated for a max peak-to-peak voltage of 400 Vpp on the RF electrodes. Here we describe the elements of the "RF chain" that supplies this voltage.

Our frequency source is a DDS-based synthesiser, named *Urukul*, part of the *Artiq Sinara* [<empty citation>] hardware ecosystem. The *Urukul* is operated at maximum output power, +10 dBm, and with a frequency ~ 27.8 MHz. This signal is then fed to an "ultra-low noise limiting amplifier" named *Squareatron* [<empty citation>]. The purpose of *Squareatron* is to greatly reduce the amplitude noise of the RF signal, V_{RF}, which is key to low radial mode frequency drifts, as radial mode frequency $\omega_{x,y} \propto V_{\mathrm{RF}}$ [<empty citation>]. The *Squareatron* outputs +17.4 dBm, which is subsequently attenuated by 19.5 dB. The signal is then amplified by a further 33.7 dB using a *Mini-Circuits ZHL-1-2W-S+*, high power amplifier. The signal is now +32 dBm RF power, enough to drive the trap electrodes. To impedance match the 50 Ω line from the amplifier to the small capacitance (~ 5 pF) of the trap electrodes, an LC impedance matching circuit is used. This LC circuit has a tuned resonant frequency of 27.84 MHz, and a measured Q factor of 43.8 found using a vector network analyser and fitting S11 impedance measurements. This resonant matching circuit has three main effects: it ensures good power transfer between RF input and trap electrodes via impedance matching, it steps up the

voltage to the required 400 Vpp, and it filters out RF noise and unwated harmonics due to the narrow bandpass nature of the LC circuit.

If components are chosen well, and adequately protected from environmental noise, this chain can produce the desired frequency and amplitude stable RF. Characterisations of the motional mode stability are discussed in section 3.3.3. We are still yet to fully quantify and debug the motional stability against thermal and mechanical noise, however it should be noted that other groups do opt for active stabilisation of RF amplitude through closed feedback loops [**<empty citation>**].

2.1.2   Trap DC Voltages

Voltage is supplied to the 40 DC electrodes using *Fastino*, a multi-channel DAC part of the *Artiq Sinara* hardware ecosystem [**<empty citation>**].

The ion is confined in the "operation" zone, seen in figure 2.1 c. The axial trapping is provided by electrodes DC-b5 and DC-f5, where b and f correspond to the back and front plane of the trap. The DAC provides ~ 10 V to these electrodes to produce an axial frequency of 1.6 MHz.

2.2   Magnetic Field

Stable Zeeman shifts of the ion energy levels are required for long spin coherence times (see section 3.2.2), and for low error single- and two-qubit gates. A permanent magnet array of Samarium Cobalt, Sm_2Co_17, is used in a Helmholtz configuration to create a stable magnetic field of 5.4 G. Samarium Cobalt was chosen for its low temperature coefficient of remanence, -0.03%/K.

The ion is shielded from unwanted external magnetic fields by two layers of 3 mm thick MuMetal shielding from *MagneticShields*. The factory quoted shielding factor is 546 for DC fields. Spin coherence time comparisons for the ion with and without magnetic shielding are shown in section 3.2.2.
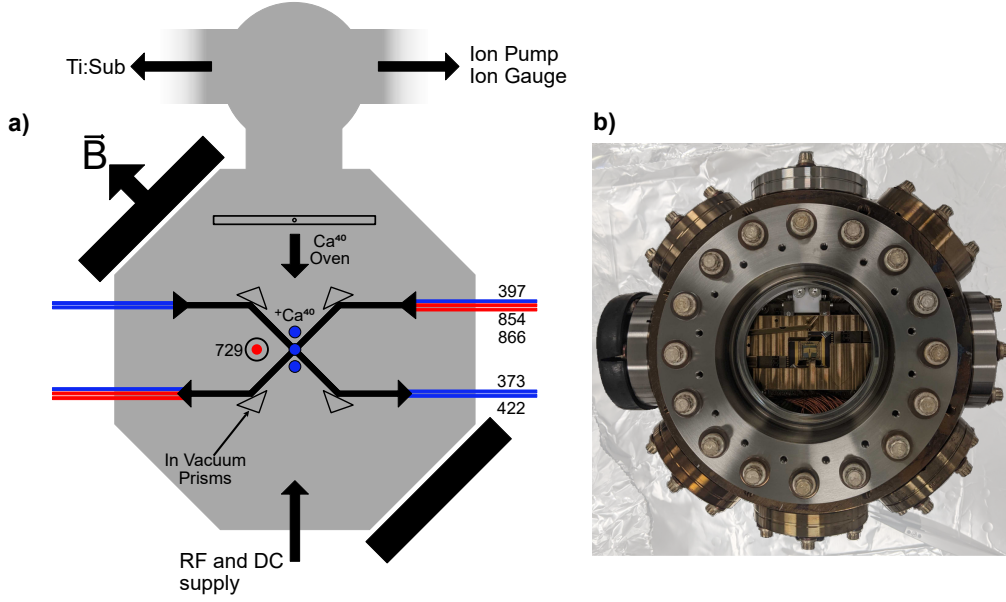
Figure 2.2: a) XXX place holder figure. I would like to replace with a solidworks render. A schematic of the vacuum chamber. Wavelengths apart from 729-nm enter through the side CF40 viewports and are directed onto the ions by in vacuum prisms. The 729-nm light enters through the larger CF100 viewports. **b)** A photograph of the assembled system prior to baking.

2.3 Vacuum System and Beam Geometry

Ultra High Vacuum (UHV) is required to extend the ion storage lifetime. However, UHV equipment is often bulky, and puts constraints on the access and visibility of the ion chain. Here we describe the designed vacuum system, and beam access. The vacuum system and beam geometries were designed by Sebastian Saner and Mariella Minder, and constructed by Sebastian Saner, Fabian Pokorny, and myself. A residual pressure of $< 10^{-11}$ mbar is desired. For this strict requirement, care must be taken in selecting in-vacuum materials, and thorough cleaning and baking procedures must be followed. A summary of tactics that were useful in the construction of the vacuum system can be found in [8, 9].

A schematic and photograph of the vacuum system can be seen in Figure 2.2. The system consists of a 6" spherical-octagonal experimental chamber[1] connected
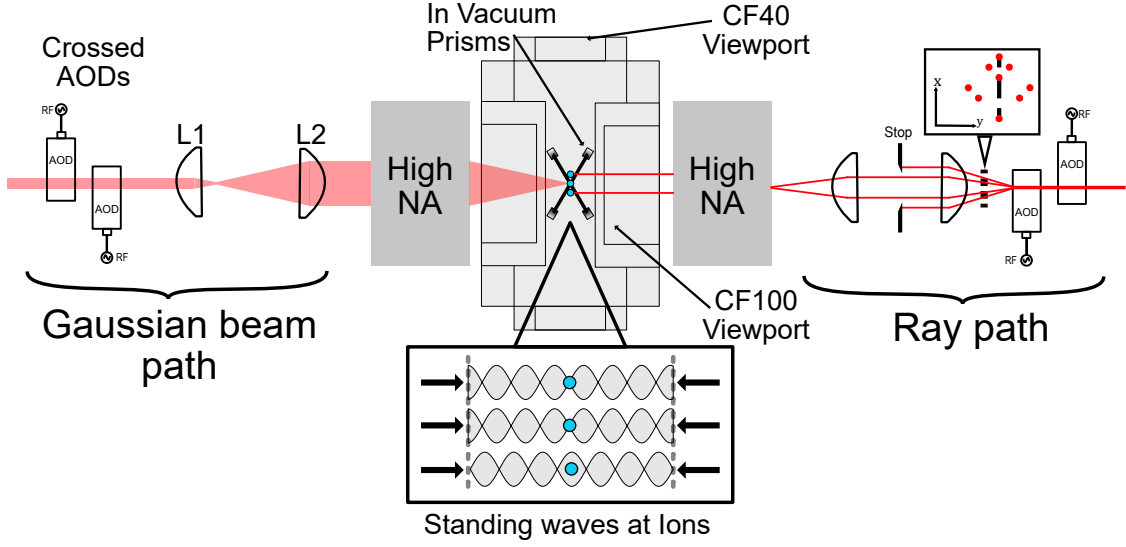
---

[1]Kimball MCF600-SphOct-F2C8

Figure 2.3: XXX Place holder figure. The standing wave single addressing system. Dual high NA objectives focus the light to a tight waist at the ions location. AODs are used to steer the light to only selected ions. The left hand side of the figure shows the Gaussian profile of the light, whilst the right hand side shows a ray representation of how two singly addressing spots are formed at the ions. L1 is a telecentric scanning lens and in combination with L2 form a beam expander.

to a spherical chamber with ion pump[2], ion gauge[3] and Titanium sublimator pump (TSP)[4] attached. The ion pump and TSP maintain the UHV to the desired $< 10^{-11}$ mbar. We find that on the ion pump alone UHV cannot be maintained indefinitely, however, firing the TSP every 4 weeks with 41 A for 60 seconds provides a sufficient pumping rate. At the time of system baking, a He leak test was performed, however no external leaks were found. We suspect the gradual pressure increase is either due to our use of in-vacuum optics, optics epoxy adhesive[5], or our use of soldered PCB components.

For optical access, there are two recessed CF100 viewports[6] on the two large faces of the experiment can, see figure 2.3. Recessed viewports were required due to the size of the chosen main objectives[7]. These custom objectives have an effective focal

---

[2] Agilent VacIon Plus 20 Pump
[3] Agilent UHV-24P Ion gauge
[4] Scanwel custom housing
[5] EPO-TEK 353ND
[6] UK Atomic Energy Authority P/N VPR100015
[7] Photon Gear custom Atom Imager

length of 33 mm, a working distance of 24.4 mm, and a numerical aperture, NA, of 0.6. They are coated for 397-nm and 729-nm. The consideration for dual high NA objectives is relatively unique in ion trap experiments, and was mainly motivated by previous work on fast entangling gates via standing waves [10].

There is further optical access via two CF40 side viewports[8] coated for 397-nm, 422-nm, 729-nm, 854-nm and 866-nm, seen in figure 2.2. Due to the spatial constraints from the trap assembly and high NA objectives, multiple of our beams must enter the vacuum can through these side ports. For the ion chain to be visible from these side ports, in-vacuum dielectric mirrors are used. These fused-silica mirrors are UHV rated and coated for 372-nm, 397-nm, 422-nm, 729-nm, 854-nm and 866-nm, with reflectivities of >99% for both s- and p-polarised light. Figure 2.2 shows a schematic of the beam geometries via the side ports. A limitation of this beam geometry is that due to the permanent B-field direction, it is not possible to provide pure π or $\sigma_{\pm}$ light to the ion. However for applications where strict polarisation control is needed, the beams can be incident through the CF100 viewport.

An electrical feedthrough on a CF40 flange[9] is used to supply our trap chip and atomic source oven with DC and RF voltages. As the DC cables run within close proximity to the RF supply, electrical pick up is a potential issue for our DC lines. RF leaked onto our DC electrodes will create unwanted pseudopotential which can lead to unexpected mode geometries, or required compensation field. This leakage is mitigated through an in-vacuum RC low pass filter board within close proximity of the trap chip with a cutoff frequency of 17 kHz. The trap chip is mounted onto this filter board via a custom Polyether ether ketone (PEEK) interposer with electric feedthroughs via embedded *Fuzz buttons*[10].
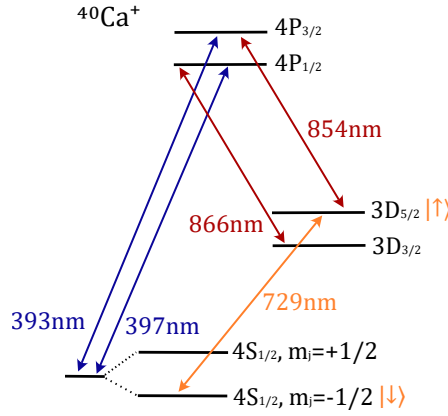
Figure 2.4: Electronic energy levels of ^{40}Ca$^+$, which will be used in this thesis. The levels are split by the Zeeman effect due to a 5.4 G external magnetic field (they are shown explicitly only for the ground state). The transitions marked are required for cooling and control over the ion. We shall use the optical-qubit with a quadrupole transition at 729-nm. XXX add zeeman sublevels for D5/2.

2.4 Ca$^+$ Laser Systems

Singly-charged group 2 elements are popular in ion trap experiments due to their single outer electron resulting in Hydrogen-like energy levels. In this thesis we use ^{40}Ca$^+$.

^{40}Ca$^+$ has no nuclear spin giving the (relatively) simple level structure shown in figure 2.4. The external magnetic field of 5.4 G is applied to split the levels via the Zeeman effect. The relevant laser transitions used in our apparatus are indicated. A zero nuclear spin isotope of calcium was chosen due to this simple level structure without hyperfine splitting. The greater number of levels due to hyperfine splitting lead to more decay paths and therefore greater complications in both cooling and gate schemes. However, due to the lack of hyperfine structure, there are no available magnetic field insensitive transitions, which are often used in ion trap experiments to further decouple the ion from a noisy environment [**<empty citation>**].

We define our qubit by the quadrupole transition at 729-nm, which we describe in section 3.1.

---

[8]LewVac ZFSVP-DUV-40CF-OUM

[9]Allectra custom

[10]Custom Interconnects

Access to other excited levels, outside of our defined two level system, are crucial for ion trap quantum logic to enable qubit readout via state selective fluorescence (397-nm, and 866-nm transitions), and state preparation via optical pumping (397-nm, 866-nm, and 854-nm transitions). Details on these schemes are given in chapter 3. Access to two additional transitions in neutral calcium for isotope selective ionisation, 422-nm and 372-nm, is also required [**\<empty citation\>**].

These transitions (apart from the 729-nm) are all driven by diode lasers[11], which are frequency stabilised to a reference cavity[12] via Pound-Drever-Hall (PDH) locking. XXX should quote finesse and FSR values here. PDH locking is used to ensure that laser frequencies are stable to <1 MHz level, well below the natural line widths of all the dipole transitions listed above. The laser frequencies are continuosly monitored with a wavemeter[13].

Frequency and amplitude control for all lasers is achieved via acousto-optic modulators (AOMs) which are driven by Artiq integrated DDS chips, *Urukuls*. The AOMs are used in a double pass configuration to allow shifts of the laser frequency by $\pm \sim 100$ MHz, with no signicant angular shifts or loss of fibre coupling.

2.4.1 Narrow Line Width 729 Laser

Lasers are a key tool for creating the highly localised, strong electric field amplitudes and gradients needed to drive both carrier and sideband transitions of the trapped ion.

As shown in Figure 2.4, two sublevels within the $4S_{1/2}$ to $3D_{5/2}$ manifolds define the qubit. This is an electric quadrupole transition as $\Delta l = 2$. For the Calcium ion this transition is at 729-nm, and so a near resonance 729-nm laser is used to implement single- and multi-qubit gates (sections 3.2.4 and 3.5). This transition is also used after Doppler cooling for resolved sideband cooling to prepare the motional mode close to its ground state (as discussed in section 3.3.1). This transition is narrrow linewidth due the the long lived $3D_{5/2}$ level, and so, for power efficiency, a

---

[11]All Toptica diodes. Red lasers: MDL DL pro; Blue lasers: MDL DL pro HP; 372-nm: iBEAM-SMART-375-S

[12]Stable Laser Systems SLS-6010 4-Bore Cylindrical Cavity

[13]HighFinesse WS7

narrow linewidth laser must be used. For the "fast entangling gates" use-case, high intensity electric-fields are required at the ion to drive sideband transitions, this will be discussed further in the single-addressing and two-qubit gate sections, but here it is sufficient to say we require >100 mW of light at the ion plane. Here we describe the 729-nm system consisting of a Ti:Sapph laser system pumped with by an Nd:YAG 532-nm laser.

An *M2 Solstis* Ti:Sapph [**<empty citation>**] is pumped via 18 W of 532-nm light from a *Coherent Verdi-V* system [**<empty citation>**] to produce around 5W of 729-nm light. The Ti:Sapph is engineered to operate with a stable < 50 kHz linewidth [**<empty citation>**]. Ti:Sapph crystals have broadband gain profiles [**<empty citation>**], which are often exploited in research environments to create frequency tunable laser systems. We however want a narrow linewidth, single frequency laser. The *Solstis* has multiple intracavity frequency selective elements which consist of (in order of coarse frequency selectivity), a birefringent filter, a tunable Fabry-Pérot etalon, and the surrounding bow-tie cavity. For stable single mode operation, the *Solstis* employs an active "dither" servo to lock the peak of etalon transmission to one of the cavity longitudinal mode. This dither consists of periodically varying the etalon spacing with a frequency of around 20 kHz. We must be aware of this dither frequency as the phase modulation leads to the creation of sidebands on our light which can interact with the ion causing unexpected errors in gates. This dither frequency (and harmonics of it), can be observed via composite pulse experiments on the ion, however it is currently not expected to be a limiting source of error in any of the interactions we study.

As mentioned, the *Solstis* alone can operate with linewidths of < 50 kHz, however this linewidth is pushed down further by referencing the Ti:Sapph output to an ulta high finesse cavity by *Stable Laser Systems* and applying a Pound-Drever-Hall (PDH) lock [**<empty citation>**]. XXX should quote finesse and FSR values here. A schematic of the 729-nm system is shown in Figure 2.5. PDH locking requires applying two sidebands via an electro-optical modulator (EOM) to the light and directing it onto the stable cavity. The light reflected from the cavity is then
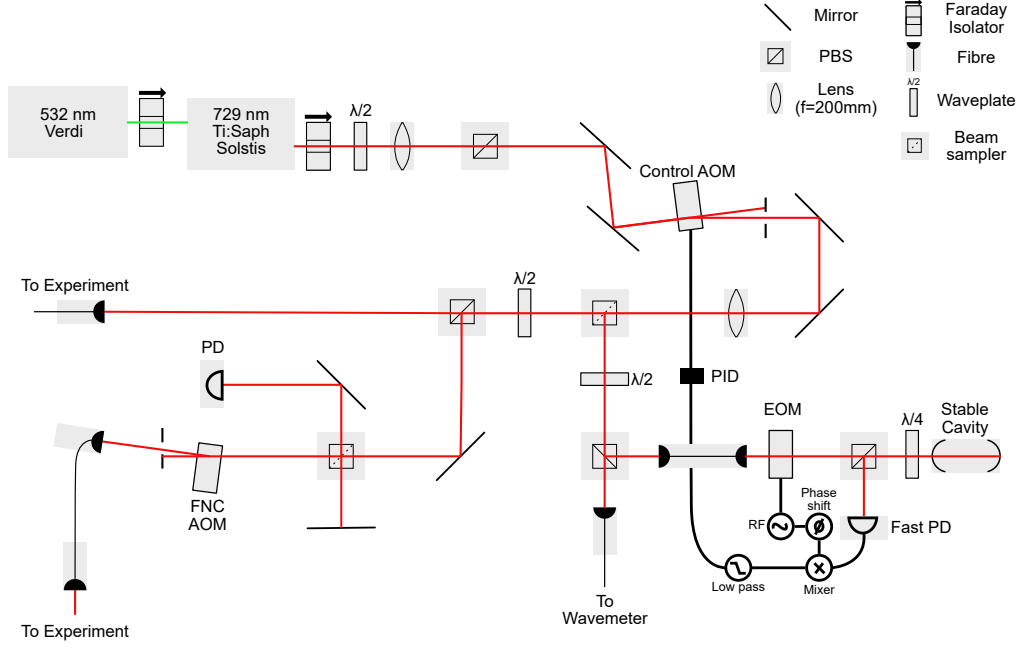
Figure 2.5: The 729-nm system. A Ti:Sapph laser tuned to 729-nm is pumped by a 532-nm source. Light is picked off at the first beam sampler to stabilise by PDH locking to a cavity.

Figure 2.6: Cavity drift over 125 days measured by reference to the ion transition. The laser offset here is with respect to running all 729-nm AOMs at their central frequencies. Outliers are due to bad fits of the ion transition frequency, not due to changes in the cavity resonance.

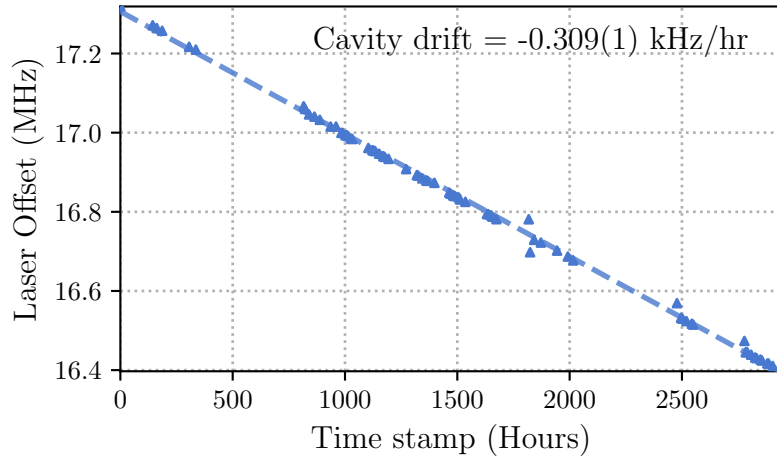directed onto a fast photodetector[14]. The reflection from the cavity consists of the interference between the carrier and the sidebands which have been respectively altered by the cavity transfer function. The photodetector signal is mixed down with the same oscillator signal as provided to the EOM but delayed by some chosen phase, and finally low pass filtered to produce a signal for use as the error signal in the servo loop. This error gives a measure for how far the carrier frequency is from the stable cavity resonant frequency and is used for feedback onto the control AOM situated after the Solstis. With this system, a linewidth of $<< 1$ kHz for the 729-nm light is expected. The electronics for this control loop are provided also by *Stable Laser Systems* in the form of their *FPGA Servo* lock box. For an effective PDH lock, both short and long term stability of the reference cavity is required. To ensure the cavity is insensitive to the environment, it is made of an ultra low expansion material. The cavity is temperature stabilised at the zero crossing temperature of 30.6°C, and is further isolated by being housed in a vacuum system at $< 1e - 7$ mbar. Long term cavity drifts of 309(1) Hz/hr are measured over 125 days, seen in figure 2.6. This measurement uses the ion as a frequency reference to probe the cavity frequency and is discussed in section A.2.

Figure 2.5 displays the other beam paths for our 729-nm system. Some light is picked off and sent to a wavemeter to continuosly monitor the frequency. However, the majority is coupled to two output fibres for our experiment and another within the group. The 729-nm light is transported from a dedicated laser lab to a the trap apparatus lab by a 10 m single mode polarization maintaining fibre. The fibre is beneficial in cleaning up the mode from the Ti:Sapph, however it can introduce phase noise due to mechanical and thermal effects along the 10 m length. To remove this introduced noise, passive stabilisation in the form of thick foam tubing along the fibre length, as well as active stabilisation by a fibre-noise-cancellation (FNC) technique [**<empty citation>**], is used. This topic has been discussed extensively in multiple PhD and Masters theses [**<empty citation>**], and so here we only quote the relevant control aspects of our arrangement. We use the *Sinara*

---

[14]Thorlabs PDA10A2

Stabilizer [**<empty citation>**] board, a dual channel PID microcontroller, with the *Pounder* [**<empty citation>**] mezzanine board, a dual channel PDH lock generator. The FNC PID software was developed by A. Agrawal [**<empty citation>**]. A comparison of spin coherence times is shown in section 3.2.2 with and without fibre noise cancellation enabled.

2.4.2   Single Addressing System

A unique feature of our system is the ability to produce single ion addressing standing waves. The design of this system is shown in figure 2.3. A single ion addressing system must be able to illuminate selected ions in the crystal whilst the others remain unperturbed. The advantage of single addressing, other than ion selectivity, is the increased intensity of light due to the tight waist at the ion location.

Our ions are separated by a distance $d \approx 5 \ \mu$m. The diffraction limited radius for a collimated 729-nm beam with an objective lens of NA = 0.6 is $\omega_0 = 386$ nm. Abberations present in real optical components will cause the addressed spot to be increasingly non-Gaussian and lead to unfavourable cross talk at the neighbouring ions. Therefore care was taken in the optical design. See I. Øvergaard Master thesis [**<empty citation>**] for relevant design considerations and rationale.

To produce more than one addressed spot and to steer the spots along the ion crystal, Acousto-Optical-Deflectors[15] (AODs) [11–13] are used. The beam deflection angle is proportional to the drive frequency supplied to the AOD. XXX could extend this section substantially.

---

[15]ISOMET OAD1343-XY-T70S

3

Experiment Characterisation

Contents

Before we can dive into running novel experiments involving the motion and spin of the atoms, the apparatus must be characterised. This allows us to both benchmark our system against state-of-the-art results, and to reveal any current limitations of the apparatus which need to be addressed.
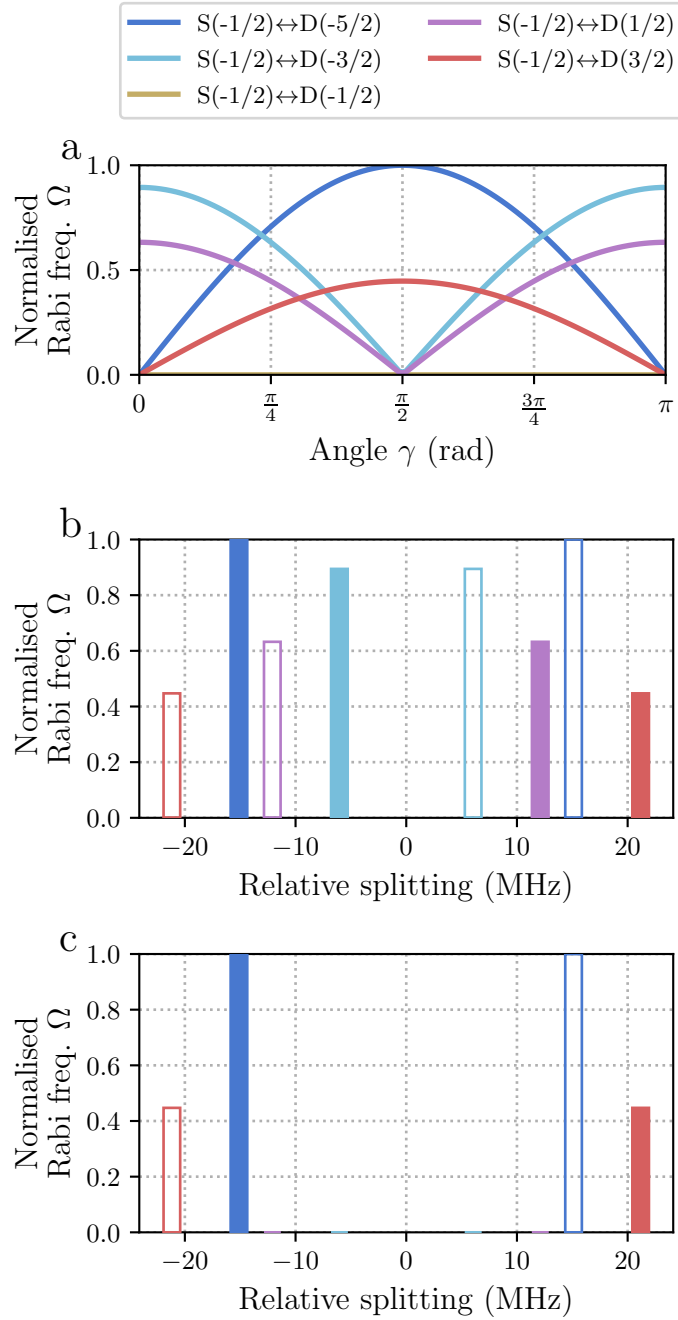
Figure 3.1: Normalised quadrupole Rabi frequencies, Ω, and frequency splittings for the $4S_{1/2} \leftrightarrow 3D_{5/2}$ Zeeman sublevels in ^{40}Ca$^+$. Solid bars correspond to transitions with lower state $4S_{1/2}$, $m_j = -1/2$, while open bars correspond to transitions with lower state $4S_{1/2}$, $m_j = +1/2$. **a)** Relative Rabi frequencies as angle γ between the polarisation vector and the magnetic field is varied. The k-vector of the light is assumed to be perpendicular to the B-field. **b)** Relative frequency splittings and strengths when $\gamma = \pi/4$. At this angle, all transitions are accessible apart from those with $\Delta m_j = 0$. This is the polarisation chosen for our initial experiments to allow access to all transitions for characterisation. **c)** Relative frequency splittings and strengths when $\gamma = \pi/2$. This is the polarisation chosen for the current and future experiments to reduce the number of transitions which can cause off-resonant interactions when the qubit defined by $4S_{1/2}$, $m = -1/2 \leftrightarrow 3D_{5/2}$, $m' = -5/2$ is used.

3.1   Quadrupole Transitions

Zeeman splitting of the $4S_{1/2}$ and $3D_{5/2}$ states leads to 2 and 6 non-degenerate sublevels, respectively. Due to the magnetic field strength of 5.4 G, the *S*-levels are split by $\sim$15 MHz, and the *D*-levels by $\sim$9 MHz. This splitting is considerably larger than both the natural linewidth of the 729-nm transition ($\sim$Hz), and the Ti:Sapph laser linewidth ($<$1 kHz), meaning the transitions can be selectively addressed by frequency tuning of the laser. There is some freedom in choosing which of these 10 possible (with $\Delta m_j \leq 2$) quadrupole transitions we define as our qubit. Each transition has a varying coupling strength, Ω, depending on the polarisation and *k*-vector of the interacting light. Here, we describe the rationale for our qubit choice of $4S_{1/2}$, $m = -1/2 \leftrightarrow 3D_{5/2}$, $m' = -5/2$.

We want excellent sideband cooling efficiency as we plan to use our motional modes considerably. For time-efficient sideband cooling, section 3.3.1, a "closed-cycle" transition is required. "Closed-cycle" here means that after one cycle of sideband cooling, the final electronic state returns with high probability back to the initial electronic state. When using such a closed-cycle transition, the next sideband pulse can be run immediately, without having to state prepare the spin again. If the $4S_{1/2}$, $m = -1/2$ state is initially prepared, then the only closed-cycle transition is $4S_{1/2}$, $m = -1/2 \leftrightarrow 3D_{5/2}$, $m' = -5/2$. Therefore this transition must be accessible, however it does not neccessarily need to be the defined qubit transition. To further narrow down our choice, we recognise the benefit in limiting the number of addressable transitions to reduce the effect of unwanted off-resonant interactions. Figure 3.1 *a*, shows the normalised Rabi frequencies of each transition as the angle γ between polarisation vector and B-field is varied, while figure 3.1 *b*, shows the relevant frequency splitting of the transitions at $\gamma = \pi/4$. These plots are for light with k-vector perpendicular to B-field, as the 729-nm addresses the ion through the main objective lens (see section 2.3). This geometry suppresses transitions with $\Delta m_j = 0$. In figure 3.1 *c*, it can be seen that at $\gamma = \pi/2$, the normalised Rabi frequency of the $4S_{1/2}$, $m = -1/2 \leftrightarrow 3D_{5/2}$, $m' = -5/2$ transition is maximised, while minimising the Rabi frequencies of all other transitions, apart
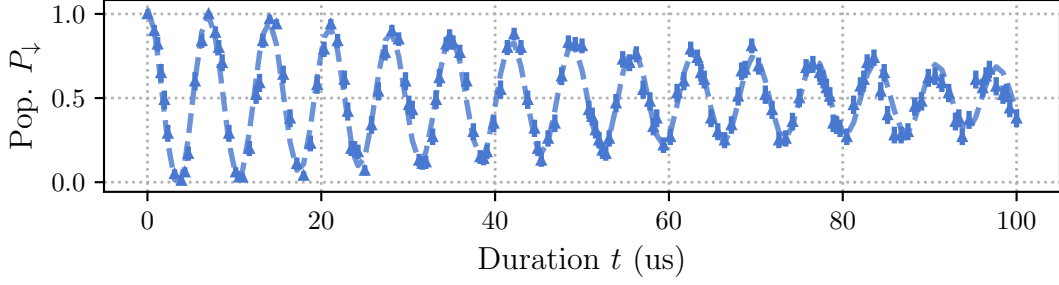
Figure 3.2: Long duration, t, Rabi flop on the qubit transition. Estimated probability of being in $|\downarrow\rangle$, $P_{\downarrow}$, at each time step using 200 individual experimental shots. Fitted dotted line using decaying oscillations model. Extracted Rabi frequency $\Omega/2\pi = 0.0716(1)$ MHz, and decay rate $\lambda = 0.0107(7)$ $1/\mu$s.

from $4S_{1/2}$, $m = -1/2 \leftrightarrow 3D_{5/2}$, $m' = +3/2$. It is worth noting that access to transition $4S_{1/2}$, $m = +1/2 \leftrightarrow 3D_{5/2}$, $m' = -3/2$ is useful for state preparation, as it allows us to optically pump from $m = +1/2$ into $m = -1/2$ ground-state.

If polarisation $\gamma = \pi/2$ is selected, now there are only two choices for qubit transition. This choice is simple as $4S_{1/2}$, $m = -1/2 \leftrightarrow 3D_{5/2}$, $m' = -5/2$ has both the larger Rabi frequency, and the lower magnetic field sensitivity, -2.80 MHz/G, compared to the $4S_{1/2}$, $m = -1/2 \leftrightarrow 3D_{5/2}$, $m' = +3/2$ transition, which has a magnetic field sensitivity of $+3.92$ MHz/G.

3.2   Spin

Discrete variable quantum computing consists of manipulating many two-level systems, which we refer to either as spins, or qubits. In this section the methods used to maniplate these spins are described, and their performances are benchmarked.

3.2.1   Rabi and Ramsey Scans

Here we briefly describe the method in which the Rabi frequencies and single qubit gate durations are extracted.

Access to $\pi/2|_x$-pulses is required for constructing the universal spin gate set [**<empty citation>**]. This single qubit gate is achieved by square pulses of 729-nm light. To roughly calibrate the required pulse length, extended oscillations are fitted using a damped oscillation model,

$$P_\downarrow = \frac{1 + e^{-\lambda t}\cos(2\Omega t)}{2}, \tag{3.1}$$

where λ is the decay rate, and Ω is the Rabi frequency.

Figure 3.2 shows one such "flop" with 1 mW of power-stabilised light, with a beam radius of ~ 15 μm at the ion. A Rabi frequency of $\Omega/2\pi = 0.0716(1)$ MHz and decay rate $\lambda = 0.0107(7)$ $1/\mu$s is found. From this a $\pi/2$ time of 1.7 μs can be estimated (note, this is on the $4S_{1/2}$, $m_j = -1/2 \leftrightarrow 3D_{5/2}$, $m_j = -3/2$ transition, which was used prior to optimising the 729-nm polarisation, see section 3.1 for more details).

The damping is likely due to a combination of out-of-Lamb-Dicke effects, and laser phase noise. The out-of-Lamb-Dicke effects are due to on-resonant terms proportional to $O(\eta^2 n)$ in the full Lamb-Dicke expansion, which may not be negligible when all modes are not cooled to their ground state. As we have not yet measured all the mode temperatures after Doppler cooling, and we have not yet characterised the laser phase noise, we do not know their relative contributions to the observed decay.

To further improve the estimate for the $\pi/2$ pulse length, the ramping time due to electronic control and AOM rise times must be accounted for. This is done by applying odd multiples of the roughly calibrated $\pi/2$ pulses consecutively, and optimising pulse durations such that the final population measurement corresponds to the Z-basis superposition state, $P_\downarrow = 0.5$, with $P_\downarrow = |\langle\downarrow|\psi_s\rangle|^2$, and ψ_s is the qubit state.

To measure the detuning of the 729-nm laser, Ramsey scans are performed. The qubit is first prepared in $P_\downarrow = 1$, next a $\pi/2|_y$-pulse is applied to prepare the $|+\rangle$ superposition. There is some delay for time t, and then a second $\pi/2|_y$-pulse is applied. If the 729-nm is on resonance with the qubit transition, then effectively

a π-pulse is performed, and the final population in $P_\downarrow$ will be 0. If the 729-nm is off-resonance, then the final population will be given by,

$$P_\downarrow = \frac{1 + \cos(\Delta t)}{2},\qquad(3.2)$$

where Δ is the detuning of the laser from resonance. The time t can be varied to increase the sensitivity to frequency offsets, and the Δ offset can be fed back to calibrate the set laser frequency.

3.2.2 Spin Coherence Times

Individual gate fidelities are ultimately limited by the loss of coherence between the the two qubit states. This can be caused either by dephasing or the natural lifetime of the upper level. By the choice of ion and qubit levels, defined between the ground $4S_{1/2}$ state and the metastable $3D_{5/2}$ state, a lifetime limited coherence time of $\tau = 1.1$ s [14] is expected. In practise coherence times are dominated by dephasing, due to imperfect tracking of laser frequency and magnetic field drifts. In characterising the spin coherence times, we hope to explore both the efficacy of the magnetic shielding surrounding the ion trap, as well as the stability of the 729-nm laser.

Practically the spin coherence times are measured by performing Ramsey experiments. Contrary to the Ramsey experiments described in section 3.2.1, we are not interested in measuring phase accumulated over time, t. Instead, the decay in Ramsey contrast over increasing delay time is measured. As such, the phase ϕ of the final $\pi/2|_\phi$-pulse is scanned, and the contrast of the resulting fringe is measured. Figures **??** show examples of such a scan. XXX Figures not added yet.

To find the cause of the decaying contrast, the laser and magnetic field noise contributions can be isolated. This is done by redefining the quadrupole qubit with varying magnetic field sensitivity transitions. Any difference in coherence times measured between these transitions will be due to magnetic field sensitivity differences exclusively.
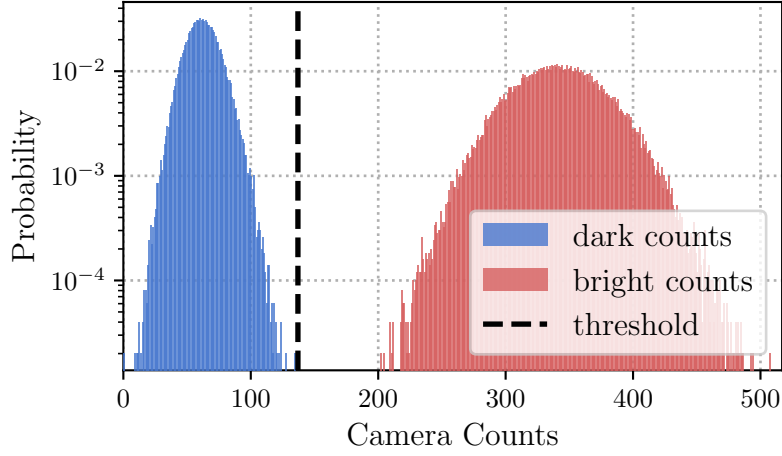
Figure 3.3: Readout histogram with 100,000 individual measurements for bright (red) and dark (blue) populations. The camera counts are presented as a histogram and fitted to Gaussian distributions to calibrate a threshold for discerning if the ion is bright or dark with the lowest probability for false measurement. Dark counts are mainly due to 397-nm light scattered from the nearest trap electrodes. With 100 μs readout time, and laser parameters set to Doppler cooling parameters, a threshold count of 137 photons is found, giving an expected statistical error of 6×10^{-9} given the fitted Gaussians.

Figure **??** shows the suppression of magnetic field noise due to the MuMetal shielding.

XXX I dont have the data I want for this story yet.

3.2.3   State Preparation and Measurement

To utilise two levels of the ion as a qubit, the ion must be able to be selectively prepared into one of the Zeeman levels of the ground state. As mentioned in section 2.2, the fixed B-field is 5.4 G, leading to a splitting between the Zeeman levels of less than 21 MHz, the natural linewidth of the 397-nm transition. This means the state cannot be optically pumped using the 397-nm frequency selectivly. Further, due to the constraint of beam geometry from the in vacuum optics, see section 2.3, the state cannot be prepared using polarisation selectivity of the 397-nm transition. Instead, the narrow line width 729-nm laser may be used on resonance with the $4S_{1/2}$, $m_j = +1/2 \leftrightarrow 3D_{5/2}$, $m_j = -3/2$ transition, and the 854-nm deshelving laser on resonance, to optically pump into the $m_j = -1/2$ Zeeman level

Parameter	Value
397-nm laser power	3 μW, $1 \times I_\text{SAT}$
397-nm laser detuning	-17.5 MHz
866-nm laser power	15 μW, $\sim 70 \times I_\text{SAT}$
866-nm laser detuning	0 MHz
Doppler cooling duration	1 ms
Readout duration	100 μs
Camera threshold	137 counts

Table 3.1: Experimental parameters used for Doppler cooling and state-selective fluorescence of the ion.

defined as the qubit ground state.

To measure the qubit state of the ion, the 397-nm and 866-nm lasers are applied for some readout duration, and the scattered 397-nm photons are counted using a camera. From the level diagram shown in figure 2.4, it can be seen that upon turning on the 397-nm laser, if the qubit is in $|\downarrow\rangle$, photons will be scattered, and if the qubit is in $|\uparrow\rangle$, then no photons will be scattered. To optimise the fidelity of measurement, it is ensured that the signal is discernible with low error from any background counts on the camera. In general, improving the number of signal counts can be achieved by tuning the 397-nm laser near to the transition resonance, by increasing the readout duration, or by increasing the percentage of scattered photons captured by the imaging system. Practically it is desirable that the readout step does not heat the motion of the ion and so the 397-nm laser is red detuned to the same setting as for Doppler cooling (see section 3.3.1). The parameters used for readout are summarised in table 3.1, and a typical histogram of readout counts for one ion can be seen in figure 3.3. The readout threshold is calibrated by taking bright counts with the 397-nm and 866-nm lasers on, and dark counts with the 397-nm laser on and the 866-nm laser off — breaking the cycling fluorescence condition. This takes the assumption that our dark counts are predominanly due to the 397-nm scattering off of nearby trap electrodes, and the 866-nm laser having a negligible contribution. With statistics from 100,000 bright and dark measurements, an expected statistical readout error of 6×10^{-9} is found, given a threshold of 137 counts and Gaussian fitted distributions. This ignores errors due to the finite
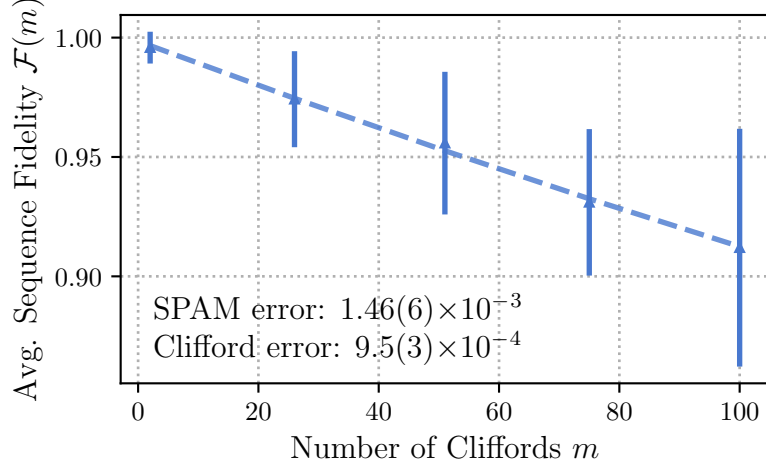
Figure 3.4: Estimating single qubit Clifford fidelities, F, and SPAM errors using randomised benchmarking. The data points are the average survival population after applying a sequence of m random Clifford gates, and a final inverting Clifford gate. The dashed line is the fit to the decay model given by equation 3.3. The error bars are given by the standard deviation of the survival populations.

lifetime of the metastable $3D_{5/2}$ level in reading out the qubit state, which will dominate measurement infidelity. The expected error due to the finite lifetime is given by $\epsilon_{\text{decay}} = 1 - e^{-t/\tau}$, which for $^{40}\text{Ca}^+$, $\tau \sim 1.1$ s, is $\epsilon_{\text{decay}} \approx 1 \times 10^{-4}$. The assumption that the metastable lifetime is limited by spontaneous decay also neglects the possibility of deshelve beam (854-nm) leakage, which is often a limiting error source [**Abaqus SPAM**].

3.2.4   Randomised Benchmarking

High fidelity unitary operations (gates) are essential for both near intermediate scale quantum computing and for reducing overheads in required physical qubits and operations in fault-tolerant schemes [15]. To evaluate the quality of both our state-preparation and single qubit rotations, randomized benchmarking (RBM) [16, 17] is employed. RBM consists of applying random combinations of a discrete set of gates to estimate an average error per gate. The single-qubit Clifford group is chosen as the set of gates to evaluate. The single-qubit Clifford group is the set of unitaries which

map the Pauli matrices to one another through conjugation. This can be thought of as the complete set of rotations of the Bloch sphere such that all valid combinations of the axis $(x \to \{\pm x, \ \pm y, \ \pm z\})$, $(y \to \{\pm x, \ \pm y, \ \pm z\})$, $(z \to \{\pm x, \ \pm y, \ \pm z\})$ are realized. There are 24 unitaries in this set. The RBM protocol is described in the thesis [18]. First the qubit is prepared in some known initial state, i.e. prepared in some chosen basis. A gate sequence is then applied which consists of multiple random Clifford gates followed by a final 'inverting' Clifford, where the 'inverting' Clifford is chosen such that the full sequence performs the identity operation. The state is then measured in the same basis to find any deviations from the identity being performed due to gate errors. This is repeated with the same preparation and sequence multiple times to calculate the probability that the identity was performed - thus giving the sequence fidelity. These steps are repeated for many different random sequences with a range of sequence lengths. The decay model used to find the fidelity versus number of Clifford gates is given by,

$$\mathcal{F}(m) = \frac{1}{2}\left(1 + (1 - 2\epsilon_{SPAM})(1 - 2\epsilon_c)^m\right), \qquad (3.3)$$

where $\mathcal{F}(m)$ is the fidelity of the sequence of length m, ϵ_{SPAM} is the state-preparation and measurement error, and ϵ_c is the average error per Clifford gate. The Clifford gates are decomposed into sequences of $\pi/2$ and π pulses about either the x- or y-axes. Up to $m = 100$ Clifford gates are probed, and the decay of the fidelity, $\mathcal{F}(m)$, is fitted using the above model. The error per Clifford is found to be $\epsilon_c = 9.5(3) \times 10^{-4}$, while the SPAM error is $\epsilon_{SPAM} = 1.46(6) \times 10^{-3}$. The decay plot for this RBM sequence can be seen in figure 3.4. The error bars are given by the standard deviation of the survival populations. There are on average 3.50 $\pi/2$ pulses per Clifford, with a typical $\pi/2$ duration of 1.3 μs.

3.3   Motion

XXX want a short introduction to the motion of the ion, and why we want to control it here.

3.3.1 Cooling

For any interaction involving the motion of the ion, we require both the ability to prepare and measure the motional state with high fidelity. For entangling gates, and the creation of squeezed states, which we consider in this thesis (although as yet unwritten), it is assumed that the motional state is prepared in Fock state $|0\rangle$. The initially trapped ions will be in some unknown high temperature thermal state. To motionally prepare these ions, first Doppler cooling is applied, and then subsequently, pulsed sideband cooling. We give a brief description of these two cooling processes here.

Doppler Cooling

Doppler cooling exploits the fact that light incident on a moving ion will appear frequency shifted in the rest frame of the ion. For Doppler cooling of ^{40}Ca$^+$, both the 397-nm and 866-nm lasers are applied. Initially the 397-nm laser is red detuned by $\sim$17.5 MHz. This results in the preferential absorption of a quanta of 397-nm light by ions with a velocity vector antiparallel to the photon k-vector. After this absorption, the ion will be in the excited $4P_{1/2}$ state and spontaneously decay to either $4S_{1/2}$, or $3D_{3/2}$ emitting a photon of either 397-nm or of 866-nm, respectively, into a random direction. The 397/866 decay paths have a branching ratio of 14.5 [**ramm_precision_2013**]. As many photon kicks are required to cool the ions, the fluorescence cycle must be "closed". To prevent the electron from beconming trapped in the metastable $3D_{3/2}$ level, the 866-nm laser is applied on resonance. The absorption and sequential emission of this 397-nm photon will lead to a net reduction in the motional energy of the ion if the emitted photon is higher energy than the photon absorbed. The equilibrium temperature is given by the condition where the Doppler cooling rate is equal to photon recoil heating of the ion. Assuming a Lorentzian absorption profile, the minimum temperature is given by,

$$T_{Doppler} \approx \frac{\hbar\gamma}{2k_B},\tag{3.4}$$

where $\hbar$ is the reduced Planck constant, γ is the natural linewidth of the transition, and k_B is Boltzmann's constant [**<empty citation>**].

For $^{40}\text{Ca}^+$, the natural linewidth of the 397-nm transition is $\frac{\gamma}{2\pi} = 21$ MHz, leading to a Doppler temperature of approximately 0.5 mK. Given a radial mode frequency of $\frac{\omega}{2\pi} = 4$ MHz, and the mean occupation number of the oscillator being given by,

$$\bar{n} = \frac{1}{e^{\hbar\omega/k_B T} - 1}, \tag{3.5}$$

the final thermal distribution is expected to have average phonon number $\bar{n} = 2.3$. Using parameters summarised in table 3.1, we find practically the final temperature after Doppler cooling to be $\bar{n} \sim 5$, although further exploration into this discrepancy is needed.

Sideband Cooling

To further cool the ions toward their motional ground state, resolved sideband cooling is used. The motion of the ion, described by a harmonic oscillator, modulates the transition frequencies of the ion, leading to sidebands at multiples of the motional frequency. For the $4S_{1/2} \leftrightarrow 3D_{5/2}$ transition, at appropriate laser intensity and motional mode frequencies, these sidebands can be resolved spectroscopically. The pulsed sideband technique employed consists of red sideband pulses, followed by deshelving, and repumping pulses on the 854-nm and 866-nm transitions respectively. An example pulse sequence can be seen in figure **??**, and experimental parameters used are summarised in table **??**. This pulse sequence and table is not yet made. To verify the efficacy of our sideband cooling, thermometry experiments are performed by driving on resonance red sideband (RSB) and π-RSB-π pulse sequences. The time dynamics of population flopping is measured as RSB pulse length is varied. In the case of Fock state $|0\rangle$, there should be full contrast RSB oscillations, and no visible oscillations on the π-RSB-π pulse. A thermal Fock state distribution (with truncation at Fock state $= 100$) is fitted to these signals to extract the mean occupation number, and $\eta\Omega$, the carrier Rabi frequency multiplied by the Lamb-Dicke parameter. A typical thermometry scan after Doppler and sideband cooling
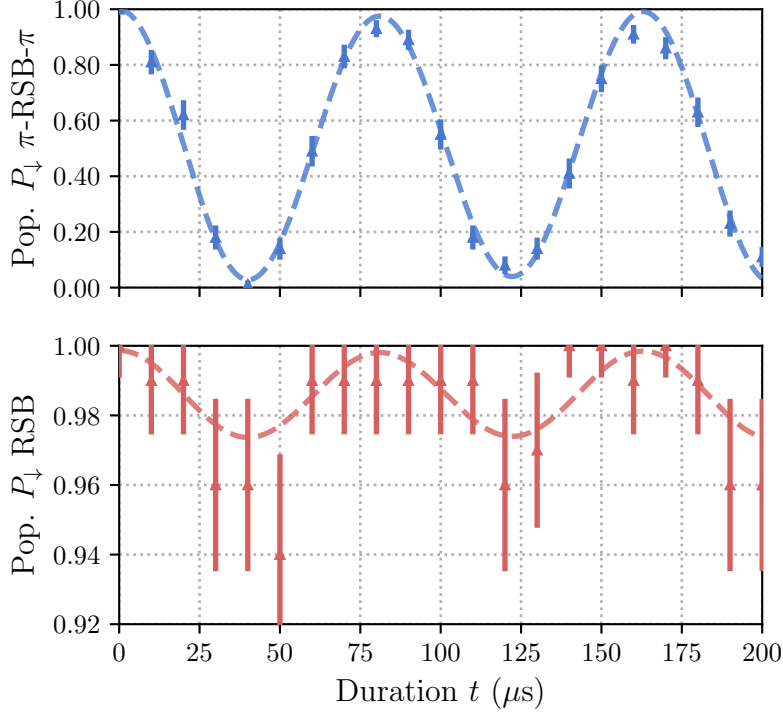
Figure 3.5: Thermometry scan after Doppler and sideband cooling. The red points are the populations measured via on-resonance red sideband, RSB, pulses, and the blue points are the populations after a sequence of π-RSB-π with varying RSB lengths. The dashed lines are fits to a thermal Fock state distribution, with truncation at Fock state $= 100$. The extracted mean occupation number is $\bar{n} = 0.03(1)$, and $\eta\Omega/(2\pi) = 73.1(4)$ kHz XXX think this number is somehow wrong.

can be seen in figure 3.5. The mean occupation number after sideband cooling is found to be $\bar{n} = 0.03(1)$, and $\eta\Omega = XX$ MHz.

Optimisation of the cooling parameters can be roughly performed by fitting temperature while scanning RSB π-pulse durations, total number of pulses, repumping and deshelving times. One can optimise for minimum temperature, however it is also important to optimise for total cooling duration. For single ion, single mode experiments, this duration is often not a limiting factor for experimental run-times, however for multi-ion crystals, any interaction involving the motion may require the sequential sideband cooling of multiple motional modes. This can not be easily parallalised due to the requirement that the RSB π-pulse is performed near resonance to one of the motional sidebands. This sequential cooling strategy
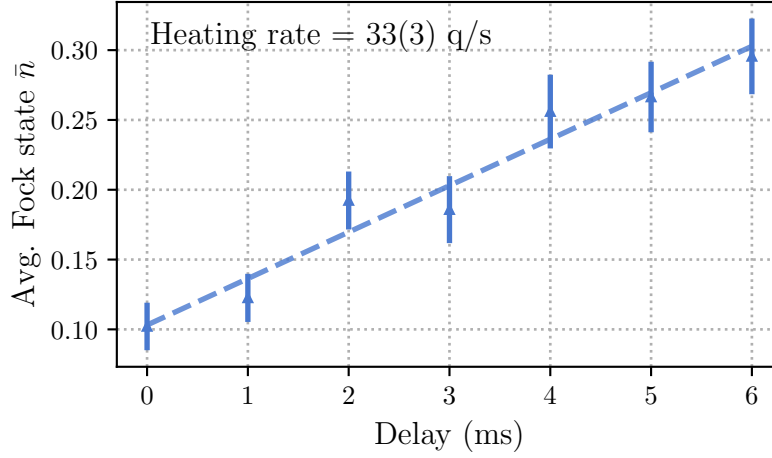
Figure 3.6: Heating rates of upper radial mode, measured by varying the delay between cooling and thermometry pulses. The dashed line is a linear fit to the data, with slope 33(3) quanta/s. The error bars are given by the standard deviation of the fitted $\bar{n}$.

can be either limiting when heating and cooling rates are comparable, or lead to prohibitive data acquisition times.

To mitigate this issue, other sub-Doppler cooling techniques with larger accepted mode frequency bandwidths may be employed. Examples are dark-resonance cooling [**<empty citation>**], electromagnetically induced transparency (EIT) cooling [**<empty citation>**], and Sisyphus cooling [**<empty citation>**]. These techniques are not yet implemented in our system, but will be likely additions once we move to larger ion crystals.

3.3.2 Heating Rates

As mentioned, the cooling of the motional modes is only relevant if heating rates are acceptably low. Heating of the motion is predominantly caused by the ion trap itself [**<empty citation>**]. This can be due to imperfections in the surface of exposed dielectric and metals causing stray fields, or can be due to noise on the DC and RF drive voltages [**<empty citation>**]. Noise due to the surface of the trap can be mitigated by increasing ion-electrode distances, or by using traps with

smaller surface area direclty exposed to the ion [**<empty citation>**]. In our case, as mentioned in sections 2.1, the *NPL* trap has an ion-electrode distance somewhat larger than most surface traps, but less than that of a macroscopic blade or rod style trap. To verify the heating rate of the system, a series of thermometry experiments were performed whilst varying the delay time between cooling and thermometry pulses. A typical plot can be seen in figure 3.6. The heating rate of the system was found to be 33(3) quanta per second on the upper radial 4 MHz mode on one ion. It is expected that the heating rate will be larger for lower frequency motional modes if electric field noise is assumed to be uniform over its spectrum [**<empty citation>**].

3.3.3 Motional Mode Stability

Due to thermal drifts and microphonics introducing amplitude and frequency noise on the RF chain, drifts of the radial motional mode frequencies are seen over time. As will be discussed in the following section 3.3.4, this can lead to dephasing of the motional state. Here the current motional mode stability is characterised, possible causes are explained, and improvements are suggested.

To measure the motional mode frequency an RF "tickle" experiment [**<empty citation>**] is performed. A short pulse of RF is applied to one of the trap DC electrodes which has a non-zero electric field projection to the mode we wish to probe. The tickle RF is scanned around the expected motional mode frequency, and when resonant, causes motional heating. This resonance is measured by observing an increase in fluorescence counts on a far red-detuned 397-nm transition. This measurement is repeated every 20 seconds, and the mode frequency is plotted over multiple hours. A typical plot can be seen in figure 3.7. XXX want to change this figure for the drifts with the box over the resonator. Assuming that in normal operating conditions the mode frequency is calibrated every 10 minutes, a standard deviation of $\sigma/(2\pi) = 870$ Hz is found. As the frequency drift cannot currently be probed over shorter time scales, we can not yet estimate the contributions of fast noise, such as microphonics, versus slower noise on thermal drift time scales.
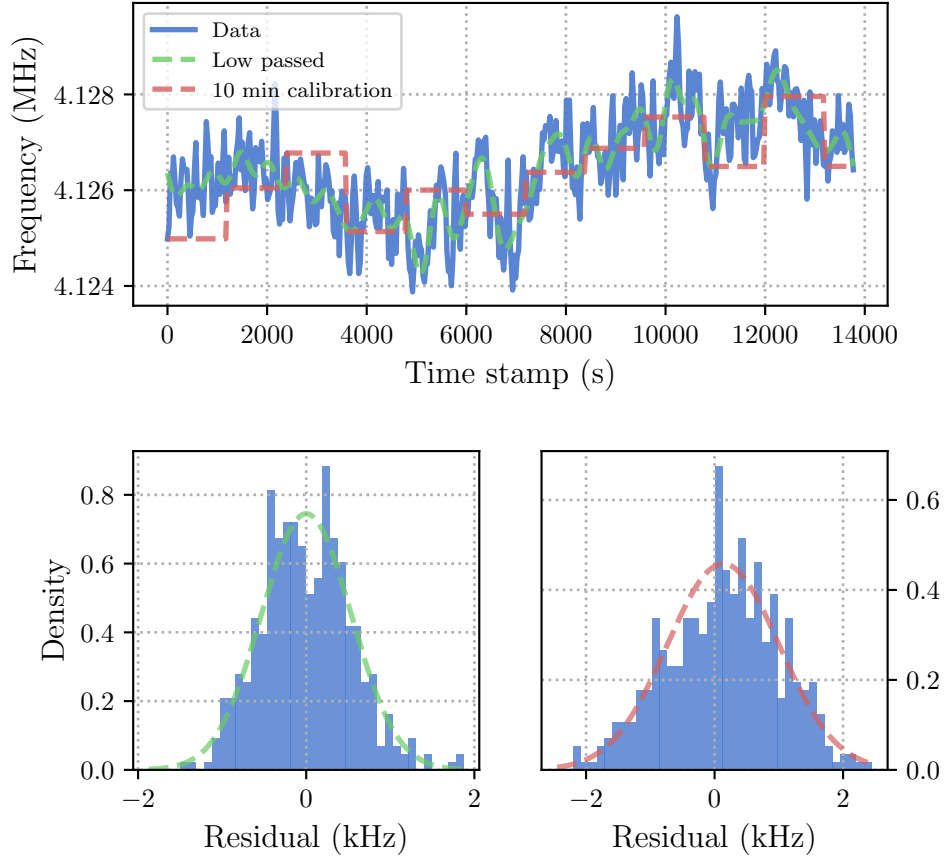
Figure 3.7: a) Motional mode frequency drift over time. The radial motional mode frequency is measured by performing a "tickle" experiment. The resulting frequency trace is shown in blue. The green line shows a low pass filter of the data, with cut-off frequency of 1.67 mHz, corresponding to an assumed 10 minutes slow thermal drift. The motional mode frequency is typically calibrated every 10 minutes, which is indicated by the red line. **b)** Residuals from the measured data and the low passed trace. The standard deviation of these residuals are due to "fast" noise which will likely not be elimated by either adding a slow active feedback loop on the RF amplitude or further isolating the resonator from temperature fluctuations. XXX replace with box data. **c)** Residuals from the measured data and expected calibrated mode frequencies. The standard deviation of these residuals suggests the typical misset detuning of the mode frequency in current experiments.

3.3.4   Motional Coherence Times

We will utilise the motional modes of the ion to store quantum information. As with the section on spin coherence times 3.2.2, the fidelity of operations, and success probability of algorithms will be limited by the coherence time of the motional state. To measure motional coherence, a Ramsey sequence is performed between states $|\downarrow, 0\rangle$ and $|\downarrow, 1\rangle$, where the first element is the qubit state, and the second element is the motional Fock state. To prepare these states the following pulse sequence is applied:

- State prepare system to $|\downarrow, 0\rangle$ via optical pumping and sideband cooling.

- Apply $\pi/2|_y$-pulse on carrier transition to prepare the qubit in $(|\downarrow, 0\rangle + |\uparrow, 0\rangle)/\sqrt{2}$.

- Apply π-pulse on the RSB to prepare the motional state in $(|\downarrow, 0\rangle + |\downarrow, 1\rangle)/\sqrt{2}$.

The full Ramsey sequence is then completed by delaying for some time t, and then reversing the above state prep and measuring spin population in $|\downarrow\rangle$.

There are two main mechanisms for motional decoherence: motional heating, as characterised in section 3.3.2, and motional dephasing due to mode frequency instability, as discussed above.

A heating rate dominated coherence time is given by, $\tau_{\text{HEAT}} = (\sqrt{e}-1)/\dot{\bar{n}}$ [**<empty citation>**], where $\dot{\bar{n}}$ is the heating rate. A dephasing dominated coherence time, consisting of the motional mode frequency drifting shot-to-shot with a standard deviation σ_ω, is characterised by a Gaussian decay profile with a coherence time of $\tau_{DEPH} = \sqrt{2}/\sigma_\omega$. Evaluating both of these models with $\dot{\bar{n}} = 33(3)$ q/s, and $\sigma_\omega/(2\pi) = 750$ Hz, the expected motional coherence times of $\tau_{\text{HEAT}} \approx 20$ ms and $\tau_{\text{DEPH}} \approx 0.3$ ms respectively, are found. From these auxiliary characterisations of the motional modes, it is expected that the coherence time will be limited by motional dephasing. However, as can be seen in figure **??**, a motional coherence time of XX(X) ms is found experimentally by fitting a Gaussian decay. XXX Figure not yet added. I want to retake motional coherence scan with the box over the resonator. Assuming this was dominated by motional mode drifts between shots, the motional

mode drift can be estimated to have a standard deviation, $\sigma_\omega/(2\pi) = 225$ Hz. Comparing this to the previously measured long-term motional mode stability, we see a discrepancy. This is likely due to the issue of time scales. The motional mode stability in the described Ramsey experiment is only relevant over the time it takes to collect enough statistics for one fringe scan, around 1 second. However, the above motional mode stability is probed only every 20 seconds and so may overestimate the instability over shorter time scales.

3.4   Spin-Dependent Forces

For full control of the spin-motion hybrid system, we require interactions that couple the two. Perhaps the simplest of this class of interactions are the red- and blue-sidebands (RSB and BSB respectively). The RSB interaction was used previously in the thermometry and sideband cooling sections 3.3.1. The RSB (BSB) consists of a single frequency laser tuned at the carrier frequency minus (plus) the motional mode frequency, ω_m. The interaction is well described by the (Anti-) Jaynes-Cummings Hamiltonian, and effectively couples spin flips with the addition or subtraction of a motional quanta depending on the initial spin state. Here, another such interaction coupling spin and motion, known as the spin-dependent force, SDF, is introduced. If the RSB and BSB interactions couple spin-motion in the motional Fock basis, then the SDF couples the two in a motional coherent basis. The SDF displaces the motional state in phase space, with a direction dependent on the spin state and an effective detuning parameter.

The optical Mølmer-Sørensen (MS) scheme [**<empty citation>**] is used to generate the SDF via a bichromatic laser field. Bichromatic refers to the simultaneous application of two tones symmetrically detuned around the qubit carrier frequency, with absolute detuning approximately equal to the motional mode frequency, $\delta \approx \omega_m$. The resulting interaction, when ignoring off resonant and higher order couplings, is given by,

$$\hat{H}_{MS} = \hbar\eta\Omega \ \hat{\sigma}_\phi \cos(\delta t) \left(a e^{-i\omega_m t} + a^\dagger e^{i\omega_m t} \right), \tag{3.6}$$

where η is the Lamb-Dicke parameter, Ω is the carrier Rabi frequency, $a(a^\dagger)$ is the lowering (raising) operator, and $\hat{\sigma}_\phi$ is the Pauli operator with ϕ being in the x-, y-plane. Applying the rotating wave approximation, and defining $\delta_g = \delta - \omega_m$, the interaction Hamiltonian can be approximated to,

$$\hat{H}_{MS} \approx \frac{\hbar \eta \Omega}{2} \, \hat{\sigma}_\phi \left(a e^{-i\delta_g t} + a^\dagger e^{i\delta_g t} \right). \tag{3.7}$$

The trajectory of this displacement can be controlled by varying δ_g: on resonance, $\delta_g = 0$, corresponds to linear trajectories, whilst off resonance, $\delta_g \neq 0$, corresponds to cyclic trajectories where after some time $t = 2\pi/\delta_g$, the motion returns to the initial state (with perhaps some phase shift). This control is exploited in both two-qubit entangling gate experiments, as well as in the creation of squeezed states.

3.4.1 Calibrating the SDF

The MS interaction is widely used in ion trap experiments due to it being robust against varying intial motional states, and to the effects of heating during the pulse sequence. However, in our use case, the SDF is sensitive to various frequency and power miscalibrations and drifts of these between calibrations. Here we describe briefly the work flow for calibrating and optimising the SDF behaviour.

In honesty, there are not many moving parts in the SDF interaction, we must calibrate the central qubit frequency, the motional mode frequency, the power in each tone, and the durations of the pulses. Complications come from the reality that the ion is a multi-level system, posseses multiple motional modes, and that experimentally each parameter can only be controlled to a certain precision.

The effect of nearby motional modes is negated by either selecting the interaction mode to be well seperated from the others either in frequency, by beam geometry, by operating the SDF near to resonance of the desired mode, or by using pulse shaping to ramp the power of the SDF and suppress the off-resonant excitation of these other modes [**<empty citation>**]. There are many tricks to either mitigate or exploit the effects of these other modes [**<empty citation>**], and we will not
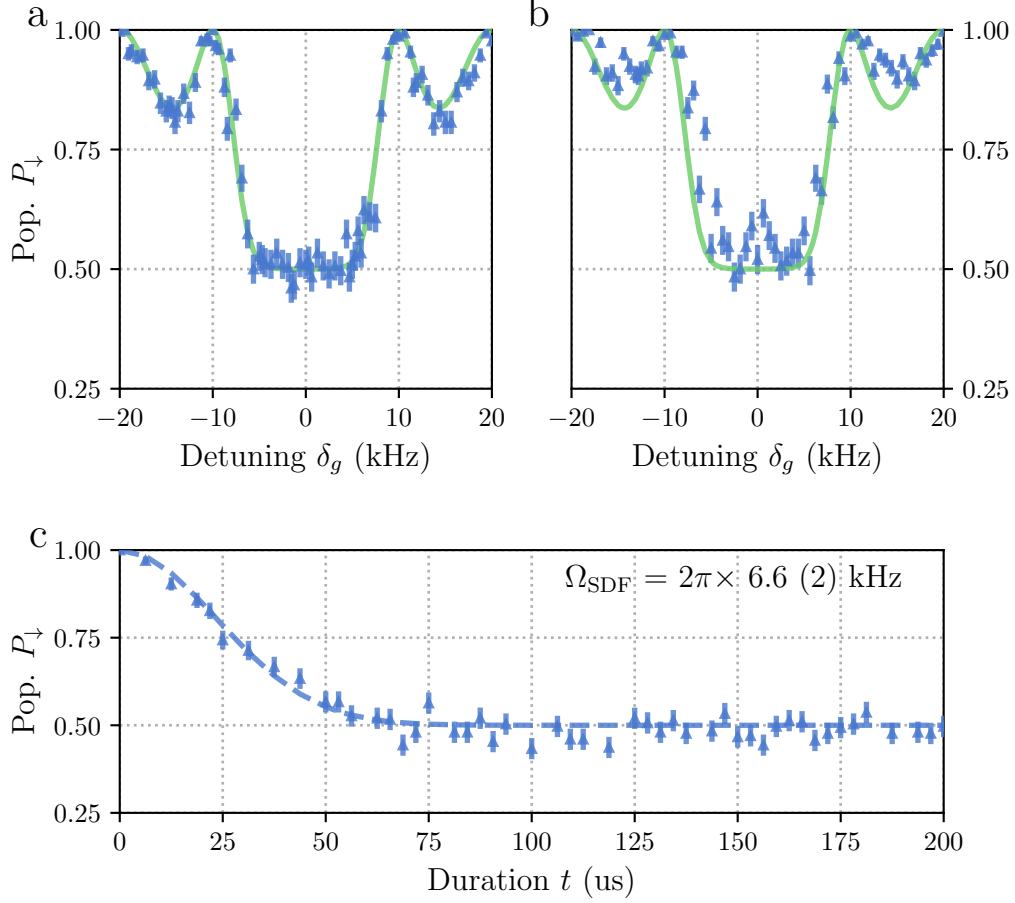
Figure 3.8: SDF traces. XXX need to update figure with legend and add caption.

go into detail here.

The power balance of the SDF tones is complicated due to our use of AOMs. AOMs generate frequency shifts in the laser beam at the expense of small frequency-dependent angular shifts. After the AOM, the beam is coupled into a single mode fibre (see figure 2.5), and so the AOMs effectively introduce a frequency-dependent loss. To calibrate the power balance, a pick off of the bichromatic beam before the ion is monitored on a high bandwidth photodiode. The beatnote contrast is measured for the two tones and the power balance is optimised by maximising this contrast.

The far off-resonant levels of our ion lead to light-shifts of our qubit frequency.

Practically to account for the light-shift the central qubit frequency must be calibrated at the optical power used for the interaction. This is done with the SDF interaction itself. When the qubit frequency is set incorrectly, the two tones will no longer have the same absolute detuning from their respective RSB or BSB. This manifests as a "skewness" of the SDF detuning trace. By varying the qubit frequency and inspecting these detuning scans, the desired SDF behaviour can be found.

To verify the behaviour of the calibrated SDF, the experimental data is compared with theory. Both "detuning" and "duration" scans are used. The "detuning" scan is performed by varying the detuning, δ_g, of the interaction, whilst keeping the SDF duration, t, constant, and vice-versa for the "duration" scan.

Figure 3.8 c shows the measured duration scan with a fit [**<empty citation>**] given by,

$$P_{\downarrow,\text{th}} = \frac{1}{2}\left[1 + e^{-4\left(\bar{n}+\frac{1}{2}\right)|\alpha(t)|^2}\right],\tag{3.8}$$

where it is assumed that the motional state is thermal with average Fock state $\bar{n} = 0.03(1)$ which is found previously from thermometry measurements. Here the displacement, $|\alpha(t)| = \Omega_{\text{SDF}}t/2$, where Ω_{SDF} is the SDF amplitude. XXX need to populate the following experimental values. These measurements were performed with a duration of XX ms, total power of xx mW, $\delta_{\text{LS}} = 2\pi \times XX$ kHz. We find $\Omega_{\text{SDF}} = 2\pi \times 6.6(2)$ kHz, from the measured fit, which is in good agreement with the expected value of $\Omega_{\text{SDF}} = \eta\Omega_{\text{CAR}}$, where Lamb-Dicke parameter $\eta = 0.05$XXX and $\Omega_{\text{CAR}} = 2\pi \times 132$ kHz XXX measured from Rabi flopping at 15XXX mW.

The detuning scan, shown in figure 3.8 a, is fitted by taking the displacement to be $|\alpha(t)| = \Omega_{\text{SDF}}\sin(\delta t/2)/\delta$. Here, a qualitatively good agreement between the measured data and the expected behaviour is seen, with the main features being the "closure" at $\delta = 2\pi/t$ where the motional state returns to the initial state, and the central flat region around $P_{\downarrow,\text{th}} = 0.5$ where the two motional wave packets are non-overlapping.

XXX need to add description of detuning scan b, where tone balance is inccorect.
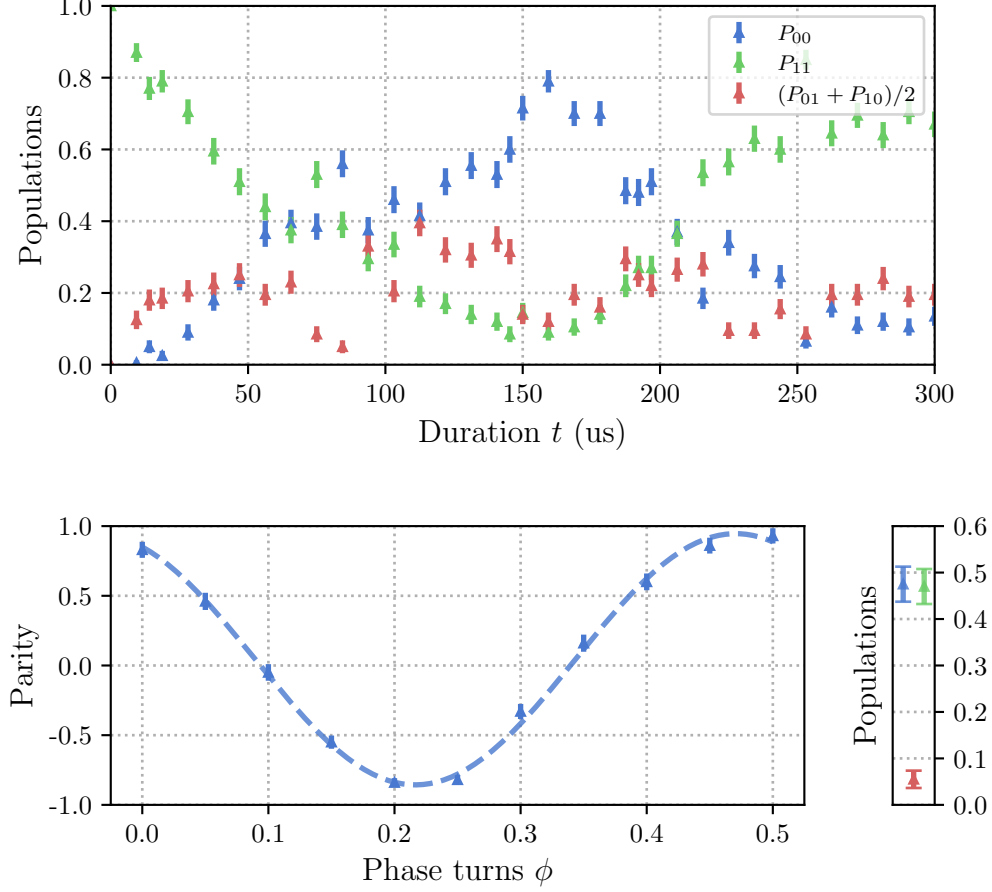
Figure 3.9: Experimental data for $\mathcal{F} = 92(2)\%$ Mølmer-Sørensen (MS) two-qubit entangling gate. **a)** Populations versus duration scan of the MS interaction. Each point corresponds to the average of 200 shots, and the error bars are given by the standard deviation of these averages. The blue points are the populations of both ions being in the $|0\rangle$ state, P_{00}, the green points are the populations of both ions being in the $|1\rangle$ state, P_{11}, and the red points are the ions being the the opposite states, $(P_{01} + P_{10})/2$. The desired entangling gate corresponds here to $t = 75\ \mu$s. **b)** Parity oscillations after the MS interaction. The parity is defined as $P_{00} + P_{11} - P_{01} - P_{10}$. The fitted contrast here is $0.90(2)$. **c)** Populations at the desired entangling gate time, $t = 75\ \mu$s.

3.5   Two-Qubit Entangling Gates

We perform two-qubit entangling gates using the Mølmer-Sørensen (MS) interaction [**<empty citation>**]. This interaction is the same described SDF from the previous section, but applied globally to two ions. The MS interaction relies on the

spin dependent geometric phase accumulated during the motional displacement [19]. To create a two-qubit entangled state, a differential geometric phase of $\pi/2$ must be accumulated between the two-qubit basis states. To ensure there is no residual motional entanglement, the final motional state must return to the initial state. In practise, using an SDF detuned by δ_g, this is achieved by applying the MS interaction for a time $t = 2\pi/\delta_g$. The MS gate is a universal two-qubit gate, and along with only single qubit gates, constitutes a universal gate set for discrete quantum algorithms.

Here we quote the current fidelity of experimentally demonstrated two-qubit gates on our system. The fidelity serves to quantify the similarity of two density matrices [<empty citation>]. For the use case of quantum information processing, what we care about is that the experimental unitary applied in the gate sequence closely resembles the unitary we desire theoretically. In general this means that the fidelity of the applied unitary should be measured in an input state agnostic way. Unfortunately, this is often not practical as the input state space can be unwieldly, and the act of preparing the input state can also be error prone. As a compromise, the unitary is tested with either one, or a set of input states, and the fidelity of the output state is measured with respect to the known target state. If the error mechansisms of the unitary are well understood, arguments can be made that this measured fidelity for a set of input state is representative (or not representative) of the average fidelity over the input state space [<empty citation>].

Here for a two-qubit entangling gate, we target the creation of the Bell state $|\Phi^+\rangle = 1/\sqrt{2}\left(|00\rangle + e^{i\phi_0}|11\rangle\right)$, from an initial state of $|00\rangle$. The fidelity between our mixed state ρ, and the pure Bell state may be given by,

$$\mathcal{F} = \langle\Phi^+|\rho|\Phi^+\rangle = \frac{1}{2}\left(\rho_{00,00} + \rho_{11,11}\right) + \frac{1}{2}\left(e^{i\phi_0}\rho_{11,00} + e^{-i\phi_0}\rho_{00,11}\right), \qquad (3.9)$$

To extract the fidelity experimentally, the popular protocol [<empty citation>], is followed where the first bracketted term of equation 3.9 is measured by performing projective measurements of the two ions after the gate sequence to extract populations, and the second bracketted term, known as the coherence terms, are

measured by applying a global analysis $\pi/2|_\phi$ pulse to the two ions and applying parity measurements. XXX define parity measurements. The contrast of the parity oscillations when varying the phase ϕ of the $\pi/2$ pulse yields the desired coherence term magnitude and phase. The creation of a Bell state is required for two qubit entangling, however, it does not matter what basis this Bell state is in, as long as it is consistent between experiments, and so the target Bell state phase may be floated. Practically this is equivalent to taking only the magnitude of the fitted parity oscillations for calculating the final fidelity, and ignoring the phase offset. The best two-qubit entangling gate fidelity currently achieved on our system is $\mathcal{F} = 92(2)\%$. As shown in figure 3.9, the magnitude of the parity scan was measured to be $0.90(2)$, while the populations $(\rho_{00,00} + \rho_{11,11}) = 0.95(2)$. Each population point in these figures are found by taking the average of 200 shots of the gate sequence.

These results serve as both a proof of principle for full spin control on our system, but also as a benchmark to which we can compare future system improvements. For future work, we will require the use of this entangling gate either as Bell state preparation for input to analogue simulation experiments [**<empty citation>**], or as a primitive gate for the spin component of hybrid algorithms [**<empty citation>**]. In both these cases, especially any use that requires multiple concatenated entangling gates, we will likely require improved gate fidelities. It is suspected that the current fidelities are limited by nearby hot motional modes, and the lack of pulse shaping in the gate sequence. We expect that with the addition of pulse shaping, the effect of nearby off-resonant transitions will be greatly suppressed, and by sideband cooling of nearby motional modes, contributions from unwanted spin-motion couplings will be negated.

4
Outlook

Appendices

A
Appendix

References

[1] Kaushal Choonee, Guido Wilpers, and Alastair G. Sinclair. "Silicon microfabricated linear segmented ion traps for quantum technologies". In: *19th Int. Confrence on Solid-State Sensors* (June 2017), pp. 615–618.

[2] Wolfgang Paul. "Electromagnetic traps for charged and neutral particles". In: *Reviews of Modern Physics* 62.3 (July 1990), pp. 531–540. URL: https://link.aps.org/doi/10.1103/RevModPhys.62.531 (visited on 08/25/2023).

[3] D. Allcock. "Surface-electrode ion traps for scalable quantum computing". In: *Ph.D. thesis, University of Oxford* (2011). URL: https://ora.ox.ac.uk/objects/uuid:bfe6d0db-092f-4661-a5c8-da3ed7ff59ff (visited on 08/25/2023).

[4] D. Kielpinski, C. Monroe, and D. J. Wineland. "Architecture for a large-scale ion-trap quantum computer". In: *Nature* 417.6890 (June 2002), pp. 709–711. URL: https://www.nature.com/articles/nature00784 (visited on 08/25/2023).

[5] Q. A. Turchette et al. "Heating of trapped ions from the quantum ground state". In: *Physical Review A* 61.6 (May 2000), p. 063418. URL: https://link.aps.org/doi/10.1103/PhysRevA.61.063418 (visited on 08/25/2023).

[6] Patrick See et al. "Fabrication of a Monolithic Array of Three Dimensional Si-based Ion Traps". In: *Journal of Microelectromechanical Systems* 22.5 (Oct. 2013), pp. 1180–1189.

[7] Guido Wilpers et al. "A monolithic array of three-dimensional ion traps fabricated with conventional semiconductor technology". In: *Nature Nanotechnology* 7.9 (Sept. 2012), pp. 572–576. URL: https://www.nature.com/articles/nnano.2012.126 (visited on 08/14/2023).

[8] K M Birnbaum. "Ultra-High Vacuum Chambers". In: *Useful Notes* (2005).

[9] J. Wolf. "Cryogenic, near-field quantum logic chips with passive field nulling on 43Ca+". In: *Ph.D. thesis, University of Oxford* (2019). URL: https://ora.ox.ac.uk/objects/uuid:df535734-dc43-487a-93de-b8789929104b (visited on 08/25/2023).

[10] S. Saner et al. "Breaking the entangling gate speed limit for trapped-ion qubits using a phase-stable standing wave". In: *arXiv* (May 2023), p. 2305.03450. URL: http://arxiv.org/abs/2305.03450 (visited on 06/26/2023).

[11] W. Nagourney. "Quantum Electronics for Atomic Physics and Telecommunication". In: *Oxford University Press* (May 2014). URL: https://doi.org/10.1093/acprof:oso/9780199665488.002.0003 (visited on 08/25/2023).

[12] Rui-Rui Li et al. "A low-crosstalk double-side addressing system using acousto-optic deflectors for atomic ion qubits". In: *arXiv* (June 2023), p. 2306.01307. URL: http://arxiv.org/abs/2306.01307 (visited on 07/03/2023).

[13] I. Pogorelov et al. "Compact Ion-Trap Quantum Computing Demonstrator". In: *Physical Review X Quantum* 2.2 (June 2021), p. 020343. URL: https://link.aps.org/doi/10.1103/PRXQuantum.2.020343 (visited on 04/28/2023).

[14] P A Barton et al. "Measurement of the lifetime of the 3d 2D5/2 state in $^{40}Ca^+$". In: *Physical Review A* 62 (2000), p. 032503.

[15] A. M. Steane. "Overhead and noise threshold of fault-tolerant quantum error correction". In: *Physical Review A* 68.4 (Oct. 2003), p. 042322. URL: https://journals.aps.org/pra/abstract/10.1103/PhysRevA.68.042322 (visited on 12/20/2022).

[16] E. Knill et al. "Randomized benchmarking of quantum gates". In: *Physical Review A* 77.1 (Jan. 2008), p. 012307. URL: https://link.aps.org/doi/10.1103/PhysRevA.77.012307 (visited on 08/25/2023).

[17] Easwar Magesan, J. M. Gambetta, and Joseph Emerson. "Scalable and Robust Randomized Benchmarking of Quantum Processes". In: *Physical Review Letters* 106.18 (May 2011), p. 180504. URL: https://link.aps.org/doi/10.1103/PhysRevLett.106.180504 (visited on 08/25/2023).

[18] A. C. Hughes. "Benchmarking memory and logic gates for trapped-ion quantum computing". In: *Ph.D. thesis, University of Oxford* (2021). URL: https://ora.ox.ac.uk/objects/uuid:3fdb0b98-3c50-483c-b66e-132495ce71af (visited on 08/19/2023).

[19] Roee Ozeri. "Tutorial: The trapped-ion qubit toolbox". In: *Contemporary Physics* 52.6 (Nov. 2011), pp. 531–550. URL: http://arxiv.org/abs/1106.1190 (visited on 03/02/2023).